

Energy-Threshold Bias Calculator: A Physics-Model Based Adaptive Correction Scheme for Photon-Counting CT

Yuting Chen^{1,2}, Yuxiang Xing^{1,2}, Li Zhang^{1,2}, Zhi Deng^{1,2}, and Hewei Gao^{1,2,*}

1. Department of Engineering Physics, Tsinghua University, Beijing 100084, China
2. Key Laboratory of Particle & Radiation Imaging (Tsinghua University), Ministry of Education, China

*Author to whom correspondence should be addressed.

E-mail: hwgao@tsinghua.edu.cn

Abstract. Photon-counting detector based computed tomography (PCCT) has greatly advanced in recent years. However, the spectral inconsistency is still a serious challenge for PCCT that could directly introduce obvious artifacts and severe inaccuracies. This work attempts to overcome the challenge by modeling the spectral inconsistency in a novel, unified, and two-term factorized framework, with a spectral skew term independent of the energy threshold, and an energy-threshold bias analytical characterization term. To solve the spectral inconsistency, a two-step decomposition algorithm called energy-threshold bias calculator (ETB-Cal) is derived here, in which the spectral skew term is grossly determined at a relatively low energy threshold and only the energy-threshold bias is needed to be calculated as the energy threshold changes. After the two terms being computed out in calibration stage, they will be incorporated into our spectral model to generate the spectral correction vectors as well as the material decomposition vectors if needed, for PCCT projection data. To validate our method, both numerical simulations physics experiments were carried out on a tabletop PCCT system. Preliminary results showed that the spectral inconsistency can be significantly reduced, for example, with a non-uniformity quantitative indicators decreasing from 26.27 to 5.80 HU for Gammex multi-energy phantom and from 27.88 to 3.16 HU for kyoto head phantom. The considerable improvements consistently demonstrate a great potential of the proposed novel physics-model based correction scheme in practical applications, as computationally efficient, calibration-wise convenient with high degree of generality, and substantially avoiding the use of X-ray fluorescence material in the energy-threshold calibration.

Keywords: Photon-Counting CT, Energy-Threshold Bias, Spectral CT, Spectral Inconsistency.

1. Introduction

Spectral computed tomography (CT) imaging has advantages of eliminating beam hardening artifacts, providing information on material composition, reducing metal

artifacts, making CT more quantitative, and so forth[1, 2]. As a breakthrough technology, photon counting detectors (PCDs) based spectral CT has attracted a great amount of attentions and intensive investigations recently[3, 4]. Different from the energy-integrating detectors used in the most of the state-of-the-art multi-detector CT (MDCT) systems, PCDs are designed to detect each individual photon and discriminate its energy, with a multi-channel readout in preset energy bins[5, 6]. In general, PCD has a smaller detector pixel size, with no electronic noise by setting the lowest energy threshold above the noise floor[7]. Overall, PCD based photon-counting CT (PCCT) can achieve higher spatial resolution, higher signal-to-noise ratio (SNR) with lower patient dose, better material discrimination capability, and more quantitative performance including K-edge imaging[8, 9].

However, to make PCCT perform consistently and robustly with a wider availability in practice, one still has to overcome quite a few serious physical and technical challenges, such as the pulse pileup, charge sharing, bias in energy threshold, and other non-ideal effects[10–14]. These effects not only cause quantum losses or readout bias, but also change the characteristics of the signal pulses in each individual detector pixel, making PCCT vulnerable to artifacts and unstable in many cases[5]. Handling of the pulse pileup and charge sharing has been actively investigated in the literature, with a tradeoff between them possible by using a subpixel binning approach [15]. This work focuses more on the bias in energy threshold, a critical factor for PCCT spectral inconsistency that has to be carefully considered in practice applications.

In PCCT, the detector can register each X-ray photon absorption event when the photon energy is above a certain threshold. This is achieved by using an electronic discriminator to directly compare the signal generated from the incident photon with an internal voltage value set by a digital-to-analog converter (DAC). As the generated signal is proportional to the photon energy, these voltage values actually determines the energy thresholds used in PCD to group the X-ray photon into different energy bins[2, 16]. In practice, unfortunately, significant bias in the energy threshold could happen, due to manufacturing imperfections in the detector electronics across pixels, along with variations in pulse heights caused by the difference in pulse processing circuits and comparators[5, 16]. Without a proper processing, such a bias will lead to not only loss in energy resolution, but also severe spectral and inconsistency, inducing obvious artifacts in reconstructed CT images and inaccuracies in material discrimination[17, 18].

For the energy-threshold bias, numerous approaches have been investigated in the literature, which can be grouped mainly into three categories, including monoenergy-based ones such as using the X-ray fluorescence materials, gamma-ray isotopes, voltage-peak, or synchrotron beams [19] to directly calibrate the DAC voltage values to ensure its corresponding energy threshold matches the monoenergy, phantom-based measurement ones where a mapping from biased PCCT data to their corresponding nominal values is directly established for correction [20–23], and model-based ones which usually consist of both calibration and correction by using a physical or mathematical model of the PCCT data[24]. Each of them has its own pros and cons[25]. Take the monoenergy-

based calibration using the X-ray fluorescence for instance, even though it is commonly used because of its simplicity, there are obvious limitations, such as the need for detector reposition and the partial-spectrum scanning, and the low count rate[21, 22, 26], making it a rather tedious and time-consuming process to find the DAC voltage values for a set of energy thresholds. For a phantom-based measurement method, it is quite straightforward to implement but its correction effectiveness could be very limited to the phantom used with a loss of good generality.

In contrary, for model-based approaches, it could achieve a relatively simple process in calibration and a highly efficient correction that works for arbitrary object to be scanned. However, the energy-threshold bias related PCCT spectral model itself has to be carefully designed through a full understanding of the PCCT imaging chain. In the literature, several model-based spectral calibration methods have been proposed before[27]. Sidky et al represented the spectra with a low-dimensional parameterization and used the Kullback–Leibler divergence between the model and the actual measured transmission fractions[28]. Based on a general nonlinear forward model, Lee et al proposed three-step estimator algorithm using a low-order polynomial approximation to estimate the basis line-integrals in a spectral distortion-model[29, 30]. However, for model-based calibration, there is still room for improvement in terms of generality and sufficiency for practical applications.

In this work, we present a robust and adaptive physics model-based energy-threshold bias calculator (ETB-Cal), which enables an analytical characterization of and rapid adaptive correction for ETBs across detector pixels, making the commonly used but practically tedious X-ray fluorescence-based calibrations unnecessary. In our previous conference paper[31], some results focusing solely on the spectral skew term were presented, while in this study, we refined the spectral model and provided a rigorous mathematical solution formulation. And several validations, especially, simulated key parameters quantitative calculation, material decomposition of head phantom and comparisons with fluorescence-based ETBs measurement and spectral correction have been conducted.

2. Method

2.1. Novel Spectral Modeling with Two-Terms Factorization

For X-ray CT using a photon-counting detector, PCD records the quantity of photons whose deposited energy falls within different energy ranges. In general, the photon count λ_i^k at the i -th pixel above the k -th energy threshold E_T^k can be modeled as,

$$\lambda_i^k = \int_{E_T^k}^{\infty} \int_0^{\infty} S_{0i}(E) H_i(E) R_i(E'; E) dE dE', \quad (1)$$

with

$$H_i(E) = e^{-\sum \mu_n(E) L_{n_i}}. \quad (2)$$

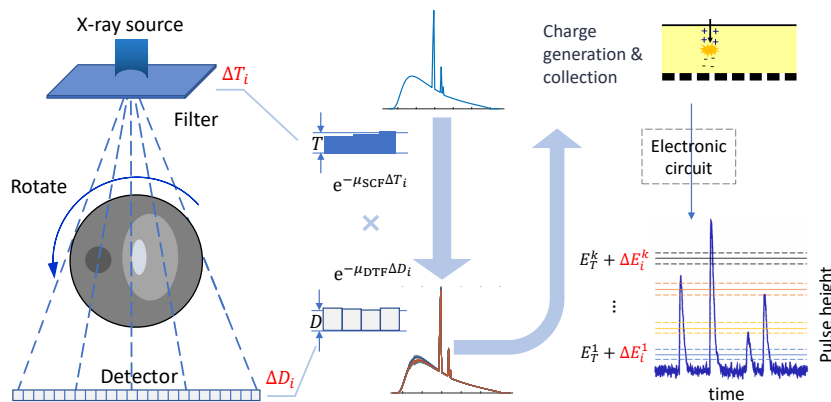


Figure 1: Schematic diagram of PC-CT counts measurement, which illustrates the sources of spectral inconsistencies in the proposed physics-based two-term factorized spectral model and the specific forms of the model parameters (ΔE_i^k and $g_i(E) = e^{-\mu_{SCF}(E)\Delta T_i - \mu_{DTF}(E)\Delta D_i}$). E_T^k is the k -th nominal energy threshold with a bias varying across different detector pixels written in ΔE_i^k , $g_i(E)$ is a spectral skew term determined by thickness deviations of two materials [$\mu_{SCF}(E)$ and $\mu_{DTF}(E)$].

Here, $S_{0i}(E)$ is the incident X-ray spectrum that can be obtained by a Monte Carlo simulations or measurements; $H_i(E)$ represents the attenuation of the object between the X-ray source and the detector with a set of $\{\mu_n(E), L_{ni}\}$, which represents the linear attenuation coefficients and the path length of X-ray through the scanned object. It can refer to a filter used for solving spectrum information, a phantom used for phantom-to-phantom calibration, or an object employed in the actual scanning process; and $R_i(E'; E)$ is the energy response of the i -th detector pixel. This classic model has been commonly used in the field of X-ray detection and measurements. For PCCT, it plays a vital role in spectral correction, material decomposition, as well as image reconstruction. In practice, however, this model itself does not explicitly take into account some key factors that could lead to significant spectral inconsistency for the detector outputs.

As illustrated in Fig. 1, two common types of spectral errors could exist in a PCCT system. One is associated with the variations of the source and detector filtrations, and the other the variations in the energy threshold. In order to take the spectral distortion and energy threshold bias into account, in this work, a novel, uniformed, and two-term factorized PCCT spectral model is proposed as follows,

$$\lambda_i^k = \int_{E_T^k + \Delta E_i^k}^{\infty} \int_0^{\infty} S_{0i}(E) g_i(E) H_i(E) R_i(E'; E) dE dE', \quad (3)$$

$$g_i(E) = e^{-\mu_{SCF}(E)\Delta T_i - \mu_{DTF}(E)\Delta D_i} \quad (4)$$

where, $g_i(E)$ is a spectral skew term as a function of thicknesses of X-ray filters but independent of energy threshold, and ΔE_i^k is a ETB term as a function of the energy threshold within the bounds of energy integration.

2.1.1. Physics behind the Two Terms It is seen that we model the spectral inconsistency by using two components ΔE_i^k and $g_i(E)$, whose physics meanings can be explained as follows.

ΔE_i^k : In general, during data acquisition a uniform nominal threshold value across all pixels will be employed. Due to various non-ideal factors in actual experimental electronic circuit, the actual measured photon-counting energy threshold exhibits deviations from the set value and varying across different pixels. We use ΔE_i^k to represent this energy threshold bias (ETB) off from their nominal ones.

$g_i(E)$: According to material decomposition theory[32], the characteristic attenuation curve of any material can be derived by a combination of that of two basis materials. In the context of the practical applications, a straightforward option is to select the pre-filter and the detector material as the two bases $[\mu_{SCF}(E)$ and $\mu_{DTF}(E)]$. From a physics perspective, the spectral skew can be attributed to the varying thickness deviations of these two materials (ΔT_i and ΔD_i) across different pixels.

2.1.2. Feasibility Analysis of Decoupling the Two Terms The two terms introduced in Eq. (3) have certain complementary equivalence when solving the model, and there is no one-step analytical solution clearly. Iteratively solving the value of the key parameters of the two terms is relatively easy but can lead to non-convergence or falling into a local optimal solution.

Fortunately, in our model, a decoupling of the two terms allows us to separate $g_i(E)$ from the ΔE_i^k with energy threshold changing out of the following considerations.

On the one hand, the energy threshold of PCD photon acquisition is positively correlated with the comparator voltage;

$$E = kV + b \quad (5)$$

the higher the voltage, the higher the corresponding photon energy, meanwhile the greater energy threshold bias. Therefore, compared to a bigger ΔE_i^k at higher thresholds, it is more reasonable to assume that ΔE_i^k is fairly small with a minimum attainable energy threshold, E_T^0 . The spectral inconsistency resulting from ΔE_i^k at E_T^0 can be considered to be overwhelmingly encompassed within $g_i(E)$.

On the other hand, the energy response of the photon-counting detector exhibits a relatively flat distribution, primarily dominated by the Compton plateau, between the accumulation of low-energy photons from various sources and the precise incident photon energy. When utilizing photon counts within this energy range to calculate $g_i(E)$, despite there might be a small error by setting ΔE_i^k to be zero, the corresponding portion relative to the total envelope area over the energy response curve will be minimal.

Therefore, based on these two observations, a reasonable and practical strategy of decoupling the two terms in order to solve Eq. (3), could be in two steps, getting $g_i(E)$ at E_T^0 first and compute ΔE_i^k at any other energy thresholds.

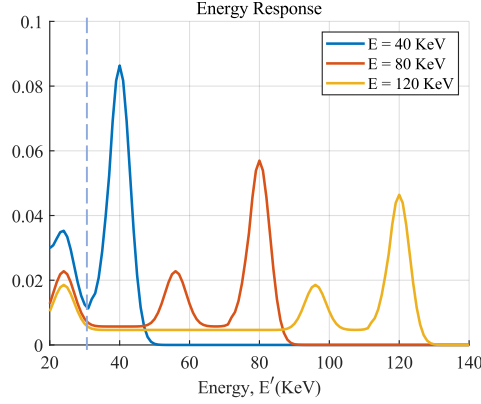


Figure 2: Energy response functions $\mathcal{R}(E, E')$, when $E = 40, 80,$ and 120 keV. Based on the decoupling of the energy threshold bias (ETB) term and spectral skew term [ΔE_i^k and $g_i(E)$], a reasonably appropriate base energy threshold E_T^0 can be selected in the low-energy range near the position indicated by dashed lines. The ETB term ΔE_i^k can be neglected for the calculation of $g_i(E)$.

2.2. Key Linearization Assumptions for Model Simplification

In order to increase the model's linearity and further simplify the model, two key considerations will be elaborated upon in the subsequent subsection.

As we know, if the value of ΔE_i^k in Eq. (3) is sufficiently small, the integral from E_T^k to $E_T^k + \Delta E_i^k$ can be approximated as the product of the interval length ΔE_i^k and the value of the integrand at E_T^k , after partitioning the integration limits, i.e.,

$$\Delta E_i^k \approx \frac{\int_{E_T^k}^{E_T^k + \Delta E_i^k} S_{0i}(E)g_i(E)H_i(E)R_i(E'; E)dE'}{S_{0i}(E)g_i(E)H_i(E)R_i(E_T^k; E)}. \quad (6)$$

Provided that the exponential term is a small quantity in Eq. (4), a first-order Taylor expansion of the exponential function can be performed as

$$g_i(E) \approx \alpha_i - \mu_{\text{SCF}}(E)\Delta T'_i - \mu_{\text{DTF}}(E)\Delta D'_i, \quad (7)$$

with

$$\Delta T'_i = \alpha_i \Delta T_i, \quad \Delta D'_i = \alpha_i \Delta D_i. \quad (8)$$

Taking advantage of these two approximations, we can linearize and simplify Eq. 3 as

$$\lambda_i^k \approx \left[\alpha_i - \Delta T'_i - \Delta D'_i \right] \begin{bmatrix} A_{1i} - B_{1i} \\ A_{2i} - B_{2i} \\ A_{3i} - B_{3i} \end{bmatrix} \begin{bmatrix} 1 \\ \Delta E_i^k \end{bmatrix} \quad (9)$$

$$\begin{aligned}
A_{li} &= \int_{E_T^k}^{\infty} F_{li}(E')dE', \quad B_{li} = F_{li}(E_i^k), \quad (l = 1, 2, 3) \\
F_{1i}(E') &= \int_0^{\infty} S_{0i}(E)H_i(E)R_i(E'; E)dE \\
F_{2i}(E') &= \int_0^{\infty} S_{0i}(E)\mu_{\text{SCF}}(E)H_i(E)R_i(E'; E)dE \\
F_{3i}(E') &= \int_0^{\infty} S_{0i}(E)\mu_{\text{DTF}}(E)H_i(E)R_i(E'; E)dE,
\end{aligned} \tag{10}$$

If the expressions for $S_{0i}(E)$, $H_i(E)$, and $R_i(E'; E)$ are provided, as well as μ_{SCF} and μ_{DTF} are selected, the value of F_{li} is then determined. These quantities are used as known coefficients to solve for α_i , ΔT_i , ΔD_i and ΔE_i^k . Once the values of the four unknown variables are determined, one can subsequently apply our spectral model to correct for spectral inconsistency involved in the PCCT experimental system.

2.3. ETB-Cal Decomposition Algorithm

To solve for the unknown parameters α_i , ΔT_i , ΔD_i and ΔE_i^k , it is necessary to generate different detector-recorded spectra which can be achieved by altering $S_{0i}(E)$ or modifying $H_i(E)$. Common approaches include varying kVp, or using filters with known $\{\mu_n(E), L_{ni}\}$ to enable the transmission measurement of the $S_{0i}(E)$, which is chosen in this work.

2.3.1. Pre-processing for the Raw Data Let $m = 1, 2, \dots, M$ represent the number of measurements with different flat filters. Define the normalized photon count as

$$\tilde{\lambda}_i^k(m) = \frac{\lambda_i^k(m)}{\sum_{i=1}^N \lambda_i^k(m)} \tag{11}$$

The denominator represents the total photon counts over an entire row of detector pixels. Such a summation in Eq. (11) as denominator eliminates individual differences in spectral inconsistencies among pixels.

This normalization offers several key necessities and benefits: it eliminates the coefficients related to ray intensity in the model's count expression, ensuring that experimental data and the model's expressions can be equated. This also helps to keep the model-solving process within a manageable range. Without self-normalization, solving for λ_i^k pixel by pixel would lead to excessive individual variation between pixels. After normalization, the focus shifts to relative errors rather than absolute ones, and the fact that $\sum_{i=1}^N \tilde{\lambda}_i^k(m) = 1$ enhances the stability of the solution.

2.3.2. Calculation for Spectral Skew Term Based on the previous elaboration and derivation, one can identify a E_T^0 where the relative impact of ΔE_i^k on the overall error

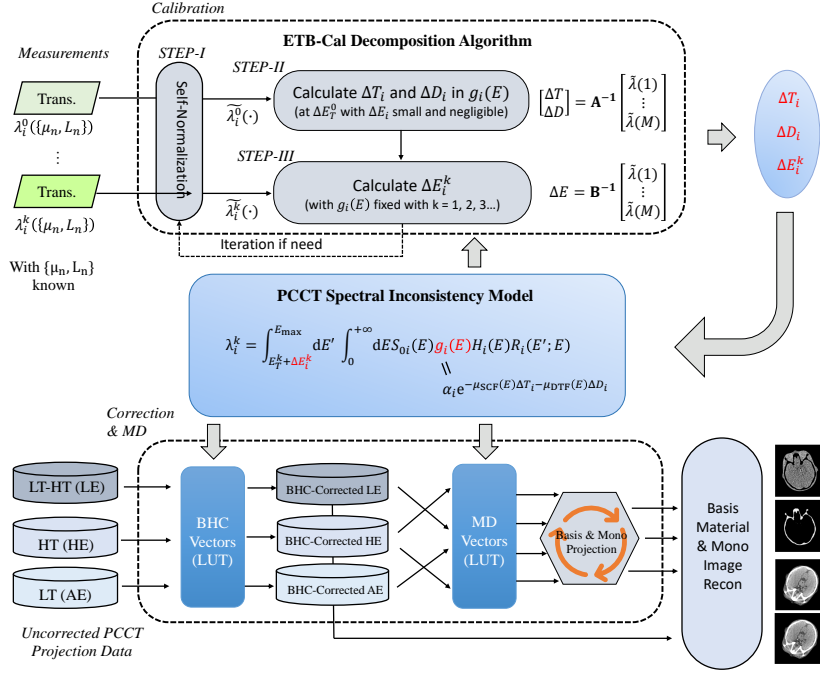


Figure 3: The overall framework of the spectral inconsistency correction. Based on the proposed spectral model, $(\Delta T_i, \Delta D_i, \Delta E_i^k)$ can determine through a series of attenuation measurements with known μ_n and L_n . By applying these parameters to the beam hardening correction process and the material decomposition process, we can correct the ring and band artifacts resulting from the spectral inconsistency in the reconstruction image, thereby enhancing the accuracy of material identification. Both the basis material and the virtual monoenergetic can be reconstructed properly.

is minimal. In other words, when ΔE_i^k in Eq.9 is a small quantity and can therefore be neglected, we get

$$\begin{aligned} \tilde{\lambda}_i^{model}(m) &= \frac{\alpha_i A_{1i}(m) - \Delta T_i' A_{2i}(m) - \Delta D_i' A_{3i}(m)}{\sum_{i=1}^N \alpha_i A_{1i}(m)} \\ &= \frac{\alpha_i [A_{1i}(m) - \Delta T_i' A_{2i}(m) - \Delta D_i' A_{3i}(m)]}{\bar{\alpha} \sum_{i=1}^N A_{1i}(m)}. \end{aligned} \quad (12)$$

Let $\alpha'_i = \frac{\alpha_i}{\bar{\alpha}}$, and

$$\tilde{v}_i(m) = \frac{1}{\sum_{i=1}^N A_{1i}(m)} \begin{bmatrix} A_{1i}(m) & -A_{2i}(m) & -A_{3i}(m) \end{bmatrix}, \quad (13)$$

by repeating M sets of X-ray transmission measurements, one can derive the following linear equations from $\tilde{\lambda}_i^{model}(m) = \tilde{\lambda}_i^{measurement}(m)$,

$$\begin{bmatrix} \tilde{\lambda}_i^{meas.}(1) \\ \tilde{\lambda}_i^{meas.}(2) \\ \vdots \\ \tilde{\lambda}_i^{meas.}(M) \end{bmatrix} = \alpha'_i \begin{bmatrix} \tilde{v}_i(1) \\ \tilde{v}_i(2) \\ \vdots \\ \tilde{v}_i(M) \end{bmatrix} \begin{bmatrix} 1 \\ \Delta T_i \\ \Delta D_i \end{bmatrix} \quad (14)$$

Once the α'_i , ΔT_i and ΔD_i in Eq. 14 are determined, only the ΔE_i^k needs to be recalculated as the threshold changes during the subsequent inconsistency correction.

2.3.3. Energy-threshold Bias Calculator We can derive the following ΔE_i^k analytical calculation formula from Eq. (3),

$$\Delta E_i^k = \frac{-\frac{\tilde{\lambda}_i}{\alpha'_i} \sum_{i=1}^N A_{1i} + A_{1i} - \Delta T_i A_{2i} - \Delta D_i A_{3i}}{B_{1i} - \Delta T_i B_{2i} - \Delta D_i B_{3i}} \quad (15)$$

Eq. (15) intuitively reflects the characteristic of this method as a calculator. ΔE_i^k can be directly calculated from an analytical expression in which all quantities are known.

When taking the transmission experiment results into account, which including several flat filter sets, the ETB could be calculated by the least squares method.

It is worth noting that, considering the linear approximation assumption for solving ΔE_i^k in section B, a reasonable approach is to set a maximum range for the possible values of ΔE_i^k . In this way, smaller incremental changes in ΔE_i^k , computed at each step, are accumulated progressively to approach the true value, which is expected to be larger. This approach effectively controls the solution error and ensures the convergence of the solution.

2.4. Benefits of the Spectral Model and ETB-Cal Algorithm

Using the two-terms factorized model, the function $g_i(E)$, derived at a specific low threshold E_T^0 , can be universally applied to all higher thresholds. As a result, for each k -th threshold (where $k = 1, 2, 3, \dots$), only one unknown parameter ΔE_i^k needs to be computed. Then spectral inconsistencies can be corrected through beam hardening correction and material decomposition vectors as shown in Fig. 3.

This spectral model and ETB-Cal algorithm significantly enhances the universality of spectral inconsistency correction while reducing computational demands, providing the following advantages. 1) Once the model parameters are determined, they can be applied universally to any scanned object; 2) The model is parameter-efficient, enabling the rapid calculation of inconsistency metrics across multiple thresholds; 3) Only a minimal amount of data is required for adaptive online calibration; 4) It bypasses the need for the complex fluorescence calibration process, simplifying implementation.

2.5. Spectral Inconsistency Correction and Material Decomposition

Once the spectral inconsistency parameters $\alpha'_i, \Delta T_i, \Delta D_i$ and ΔE_i^k are obtained, they can be incorporated into Eq. 3 to generate attenuation vectors of BHC or MD target materials. By comparing these vectors with the lookup tables that does not account for spectral inconsistency, a corresponding relationship can be derived, represented by a set of correction or decomposition coefficients.

Image-domain material decomposition was applied to the head phantom data instead of projection-domain one, as the latter exhibits high noise levels in this case. With the multi-material spectral correction (MMSC) proposed in [33], P_t and P_b respectively representing total and bone projection, a beam-hardening-free projection is derived as

$$P_{\text{dMMSC}} = P_t + g(P_t, P_b). \quad (16)$$

After two sets of low- and high- energy beam hardening free projection are obtained. One can produce basis images $\{M_1, M_2\}$ through image-domain material decomposition as

$$M_1, M_2 = \mathcal{M}_I^{-1}(\mathcal{R}(P_{\text{dMMSC}}^L, P_{\text{dMMSC}}^H)), \quad (17)$$

where \mathcal{M}_I^{-1} and \mathcal{R} are image-domain material decomposition and reconstruction operator, respectively.

3. Experiment Setup and Evaluations

3.1. Experimental Setup

The CT platform for physics experiments is shown in Fig. 4(a) and consists of three main components: a X-ray source, a carrier table, and a photon-counting detector. The Varex G242 tube with EMD high voltage EPS50RF is adopted as the X-ray source in the system, the maximum voltage of the tube is 150 kV, the maximum power is 45 kW, and the focal size is 0.4 mm - 0.8 mm. A 2 mm aluminum filter is placed between the X-ray tube and the scanned object to modulate the spectrum. The PCD used in the experiment is XC-FLITE X35, with CdTe as sensor layer material and two energy thresholds can be setup simultaneously. The detector features an Anti-charge Sharing Functionality, which aggregates the recorded energy of neighboring pixels to the central pixel, thereby exerting a certain degree of suppression on charge sharing. The detailed imaging parameters are listed in Table 1.

3.2. Numerical Simulations

To validate the rationale of the proposed spectral model and ETB-Cal algorithm, we performed precise unknowns solution values and qualitative phantom reconstructed images comparison. The simulation only involves the detector-end thickness inconsistency (ΔD_i) in spectral skew term, with $g_i(E)$ generated by $e^{-\mu_{\text{DTF}}(E)\Delta D_i}$, and μ_{DTF} selected as the linear attenuation coefficient of CdTe, which matches the detection

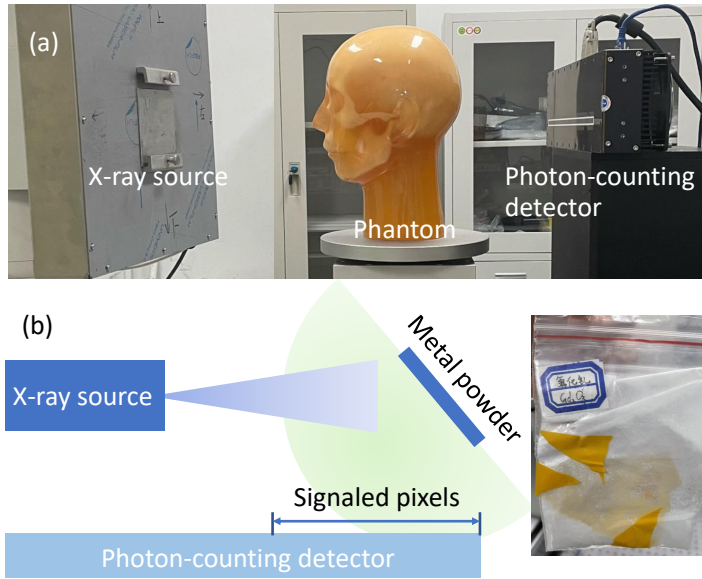


Figure 4: Experiment setup of photon counting CT: (a) Phantom experiment; (b) XRF-based calibration experiment.

Table 1: The Imaging Parameters of the Phantom Experiment.

Parameter	Value
kVp	120 kVp and 80 kVp
Detector pixel size	0.1 mm \times 0.1 mm
Sensor layer	0.75 mm CdTe
Number of detector pixel	3564 \times 64
Filters used in calibration	Al: (0.94, 2.96, 5.04, 10.53, 20.67) mm
Source to iso-center distance	750 mm
Source to detector distance	1085 mm
Acquisition frames	1080 frames / 360°
Recon size	512 \times 512
Voxel size	0.5 mm \times 0.5 mm

material in physics experiments. The distribution of ΔD_i was set ranging from -0.075 mm to 0.1 mm (total thickness of 0.75 mm in physics experiments), with a spatial high-frequency inconsistencies superimposed on global low-frequency one. The ΔE_i was randomly distributed within the range of -10 keV to 10 keV. Additionally, a comparison of the reconstructed images and profile values before and after ETB-Cal correction was performed on a virtual water phantom with four slightly denser regions in it.

Simultaneously, a set of $\{\Delta D_i, \Delta E_i\}$ was introduced on a clinical simulation projection of a abdominal phantom to qualitatively compare the correction performance of the direct inversion method, the ETB-Cal algorithm, and the ring removal method using polar coordinate filtering.

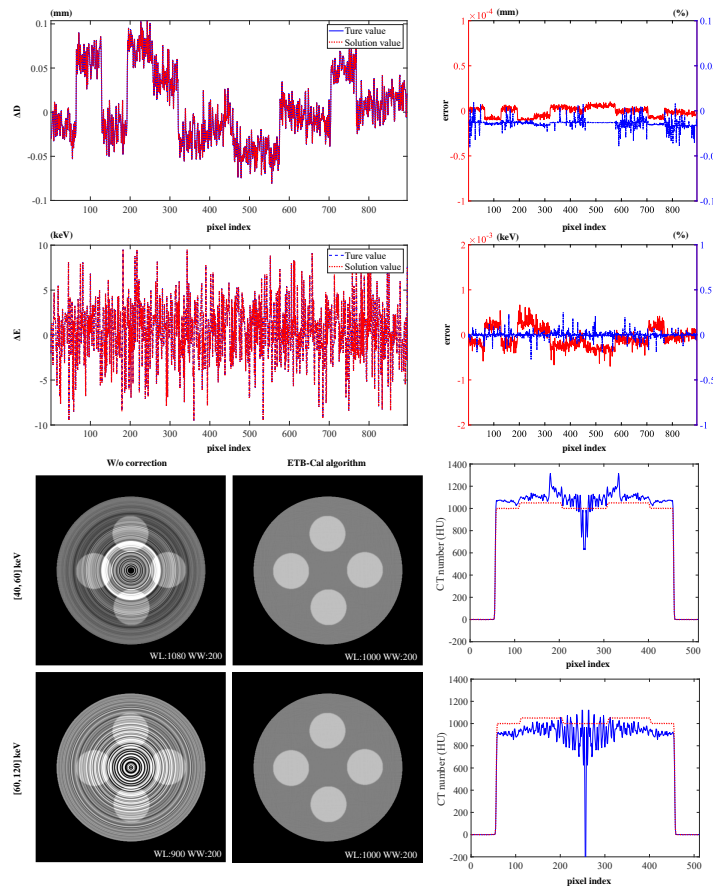


Figure 5: The ΔD_i (selected as CdTe, same with XCounter FX35 detection) distributed from -0.075 to 0.1 mm, which accounts for both inter-module and intra-module random variations (with whole detection thickness of 0.75 mm in physics experiment), and the ΔE_i from -10 keV to 10 keV were incorporated to validate the algorithm's effectiveness. Both the absolute and relative errors in the solutions of ΔD_i and ΔE_i were minimal, and excellent results were achieved in correcting inconsistencies in the reconstructed images of a virtual water phantom containing four slightly denser regions, without the addition of noise.

Especially, the direct inversion method utilizes the two linearization approximation assumptions outlined in Section II.B, treating the parameters in two spectral inconsistency terms as unknowns to be solved simultaneously. Under the constraint that ΔE_i has a defined range for a single solution, the method incrementally accumulates the computed values of ΔE_i from each step and applies a least-squares approach for multi-step unknown solving.

3.3. Physics Experiments

The phantom used in the physics experiment are kyoto head phantom and gammex multi-energy phantom. Through data pre-preprocessing and rebinning of every 4 pixels

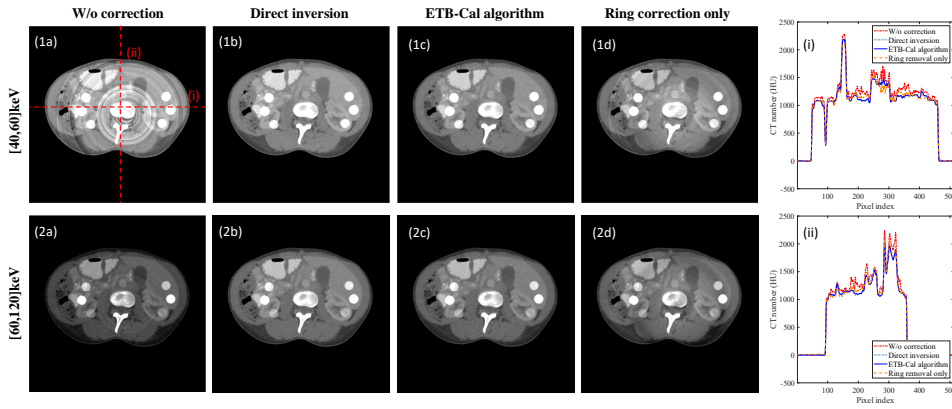


Figure 6: Reconstruction results of simulation abdomen phantom: (a) with no calibration; (b) with direct inversion calibration; (c) with ETB-Cal algorithm calibration; (d) with only the ring removal method calibration. Last column is middle row and column in low-energy reconstruction image. Display window: [800, 1400] HU.

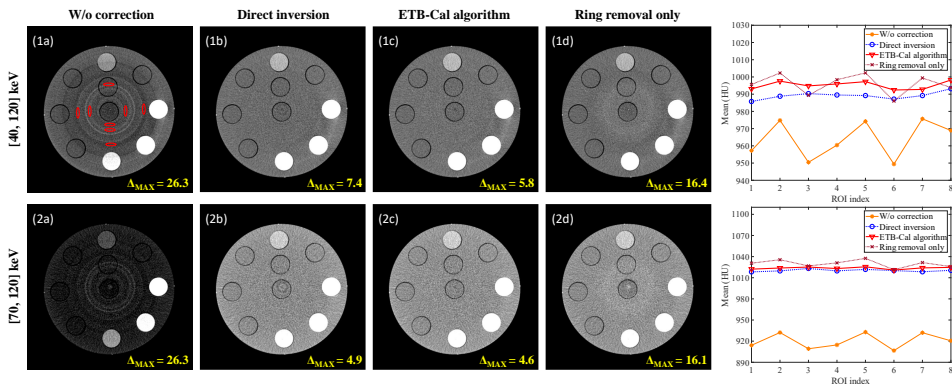


Figure 7: Reconstructed images of Gammex Multi-energy phantom : (a) without calibration (b) with direct inversion calibration (c) with ETB-Cal algorithm calibration (d) with only the ring removal method calibration. The results of two rows come from two different low and high photon energy range of collected X-ray photons. Total of 8 selected ROIs are marked in (1a). Display window: [890, 1130] HU.

in the detector column direction and rebinning along the detector row direction,, we ultimately obtained a single-frame photon-counting dataset with dimensions of 896 by 1.

There are several non-ideal factors in the practical experiments, such as pulse pileup, charge sharing, and scatter, particularly in large phantoms. Enabling the anti-charge-sharing (AC) mode exacerbated the pulse pileup effect compared to when the mode was disabled, likely due to the extended charge integration time required to collect charges from adjacent pixels. Conversely, disabling the AC mode resulted in a significantly larger pulse pileup. To minimize pulse pileup and mitigate charge sharing, we opted to keep the AC mode off, while setting higher thresholds and a lower current. Additionally, a

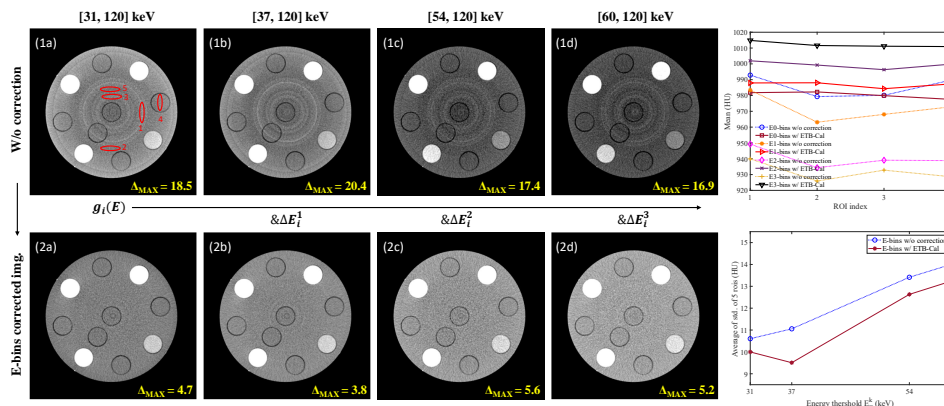


Figure 8: Reconstruction results before and after calibration with ETB-Cal algorithm under four energy threshold set. The data of 31keV to 120keV energy range was selected to obtain the $g_i(E)$ to be used, making only ΔE_i^k ($k = 1, 2, 3$) need to be solve when it comes to other three sets of data with different energy ranges. Column (a) - (d) show data of different energy ranges. Display window: [860, 1100] HU.

relatively low tube current was used to suppress flux-related effects, such as pulse pileup. In subsequent experiments, both counting modes (AC OFF and AC ON) were employed in the Kyoto head phantom experiment for a comprehensive comparison of the imaging results. For all other cases not specifically mentioned, the AC OFF mode was used.

3.4. Evaluations

To quantify the performance of spectral inconsistency reduction by the ETB-Cal algorithm, we selected some regions of interest (ROIs) in the E-bins reconstruction images that should be uniform for statistical quantification of image value uniformity. We measure the maximum difference of CT numbers among selected ROIs of the object, i.e.

$$\Delta_{\text{MAX}} = \max(\mu_i) - \min(\mu_i) \quad (18)$$

where i is the index of the ROIs and μ_i is the averaged value in HU inside the i -th ROI.

To assess the impact of the ETB-Cal algorithm on the noise in the reconstructed images, we also calculated the standard deviation (σ_i) within the selected ROIs. When comparing the σ_i of the original and ETB-Cal corrected images, the σ_i of the original image was scaled proportionally based on the alignment of its μ_i with that of the ETB-Cal corrected image.

4. Results

4.1. Numerical Simulations

As shown in Fig. 5, the absolute error of ΔD_i is within 2×10^{-5} mm, with the relative error smaller than 0.05 %. The absolute error of ΔE_i is within 1×10^{-3} keV, and the

relative error is within 0.3 %. Similarly, a few outliers in the relative error of ΔD_i and ΔE_i are caused by the true value of them being close to 0. From the reconstructed images of the virtual water phantom and the corresponding profile plots passing through the center, it can be observed that the severe artifacts caused by the predefined spectral inconsistency have been completely removed.

As shown in Fig. 6, the direct inversion method mitigates visually noticeable artifacts in most regions of the low-energy reconstructed image shown in (1b). However, in areas near the image center where inconsistencies are more pronounced, the correction effect is not significant enough. The ring removal method only partially addresses ring artifacts and fails to deal with the overall CT value shift leading to band artifacts. In contrast, ring and band artifacts are no longer visible in ETB-Cal algorithm corrected images shown in (1c) and (2c), and the profile plots of the middle-row and middle-column exhibit significantly smoother results.

4.2. Physics Experiments

4.2.1. Gammex multi-energy phantom To facilitate the display and comparison of removal effects on the artifacts caused by spectral inconsistency, eight regions of interest (ROIs) distributed across different brightness levels of the ring bands were selected in Fig. 7 to compute Δ_{MAX} . For the [40, 120] keV energy range, the Δ_{MAX} values after correction with the direct inversion method, ETB-Cal algorithm, and ring removal method decreased by 71.78 %, 77.93 %, and 37.78 %, respectively, compared to the reconstructed E-bins images without correction. Similarly, for the [70, 120] keV energy range, the Δ_{MAX} values after correction with the direct inversion method, ETB-Cal algorithm, and ring removal method decreased by 81.45 %, 82.60 %, and 38.63 %, respectively.

Then we moved on to the practical multiple-energy threshold application of ETB-Cal algorithm. Specifically, the photon counting detector used in the experiment can only set two thresholds in a single acquisition. After aligning the first projection angle, data from two acquisitions were utilized, with thresholds set at 31 keV and 54 keV for the first acquisition, and 37 keV and 60 keV for the second one. Fig. 8 shows the reconstruction images before and after ETB-Cal correction under four different thresholds. It can be observed that the ETB-Cal algorithm exhibits significant spectral correction and ring removal effects on all these thresholds, corresponding reducing magnitudes of 74.63 %, 81.65 %, 67.73 %, and 69.27 % in Δ_{MAX} , respectively.

At threshold settings of 37 keV and 60 keV, the corrected images still show a noticeable narrow dark band near the center. This could be attributed to non-ideal factors such as polarization and detector temperature drift between the two data acquisitions, leading to localized errors that cannot be fully corrected by energy threshold bias ΔE_i alone that well.

Additionally, we calculated the standard deviation within five selected ROIs and used $\bar{\sigma}_i$ to characterize the noise levels before and after correction. It can be observed

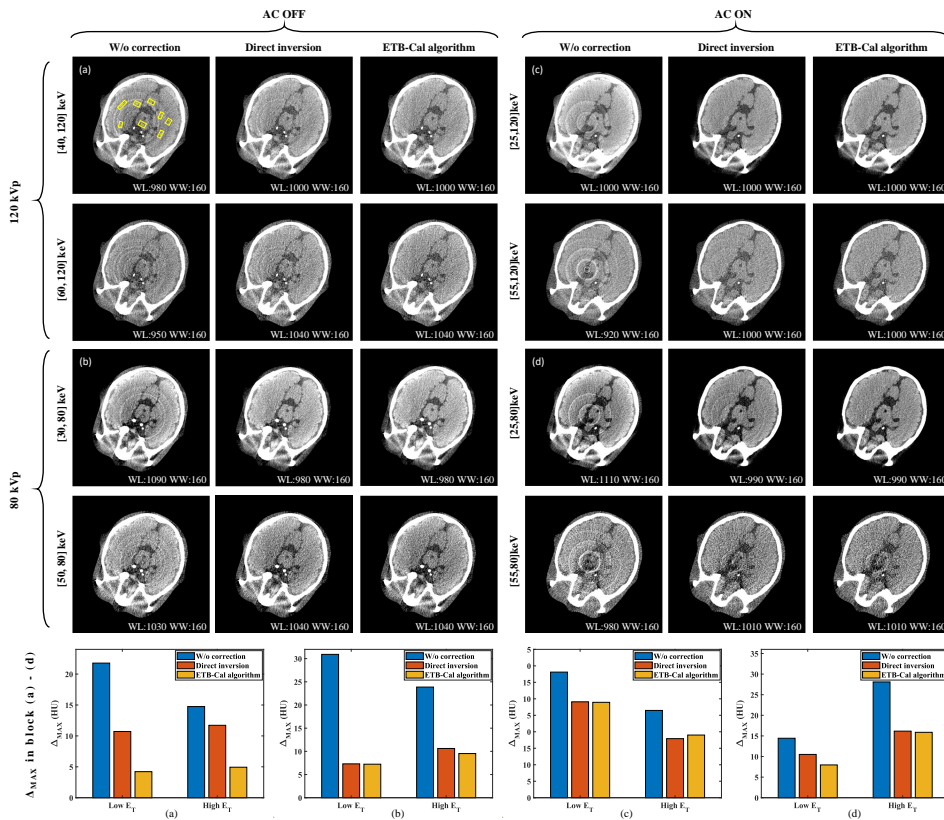


Figure 9: Reconstructed images of Kyoto Head phantom under 120 and 80 kVp and four different threshold set before and after calibration : (a) 120kVp, threshold: 40, 60 keV, AC OFF (b) 80kVp, threshold: 30, 50 keV, AC OFF (c) 120kVp, threshold: 25, 55 keV, AC ON (d) 80kVp, threshold: 25, 55 keV, AC ON. And the results of Inconsistency of kyoto head phantom under different experiment conditions.(unit: HU)

that, under the ETB-Cal algorithm, the noise levels in the corrected images remain nearly the same as uncorrected images. Moreover, due to the removal of a few outliers corresponding to ring artifacts, the $\bar{\sigma}_i$ exhibits a slight decrease across different threshold settings compared to the without correction ones.

4.2.2. Kyoto head phantom We performed inconsistency correction using both the direct inversion and ETB-Cal algorithm on kyoto head phantom data acquired under total four combinations of different kVp settings and whether or not the detector's built-in anti-charge-sharing (AC) module was enabled. The results show that the ETB-Cal algorithm provides significantly better correction performance than the direct inversion one, effectively eliminating ring artifacts in the original images in most cases. However, in the AC ON mode, some regions of the artifacts were not fully removed, likely due to the increased circuit processing time per scan caused by the activation of the AC module, which exacerbated time- and count-related non-ideal factors such as pileup (note that all our experiments were conducted with the AC OFF mode). In addition to

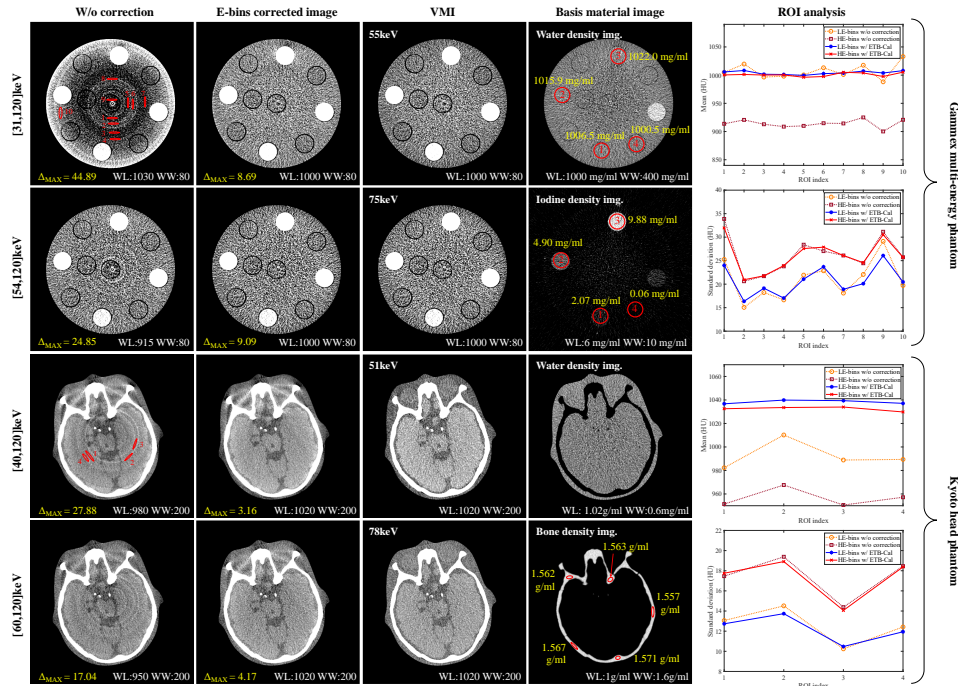


Figure 10: Material Decomposition result of Gammex ME Phantom under 120kVp and the threshold set of 31keV and 54keV in the upper half of the figure, and kyoto head phantom under 120kVp and the threshold set of 40keV and 60keV in the lower part of the figure. The iodine concentrations within the three iodine rods are 2, 5, and 10 mg/ml. The ROIs has been marked on the reconstruction images.

qualitative image comparisons, we performed Δ_{MAX} quantitative analysis in selected 8 ROIs (marked with yellow lines in the top left reconstruction E-bins image), with the results shown at the bottom of Fig. 9. Especially, under the conditions of block (a) with 120 kVp and AC OFF, the E-bins image obtained from the [40,120] keV energy range data achieved a Δ_{MAX} value below 5 HU after ETB-Cal correction.

4.2.3. Material decomposition For the phantom data to be performed material decomposition, we also compared the Δ_{MAX} on the E-bins images before and after ETB-Cal correction among the selected ROIs marked in the figure. For multi-energy phantom of [31, 120] and [54, 120] keV photon energy, Δ_{MAX} decreased by 80.64 % and 63.46 %. For head phantom of [40, 120] and [60, 120] keV photon energy, Δ_{MAX} decreased by 88.68 % and 75.53 %, respectively.

As shown in Fig. 10, the reference iodine concentrations in these three iodine rods marked in the basis images of multi-energy phantom in are 2, 5, and 10 mg/ml, respectively. Meanwhile, the estimated iodine concentrations are 2.07, 4.90, and 9.88 mg/ml. The prominently brighter rod in the water basis image contains calcium as the mixture.

It can be seen that bone and soft tissue of the head phantom are completely separated, and in the case of virtual monoenergy images at 51 keV and 78 keV, both

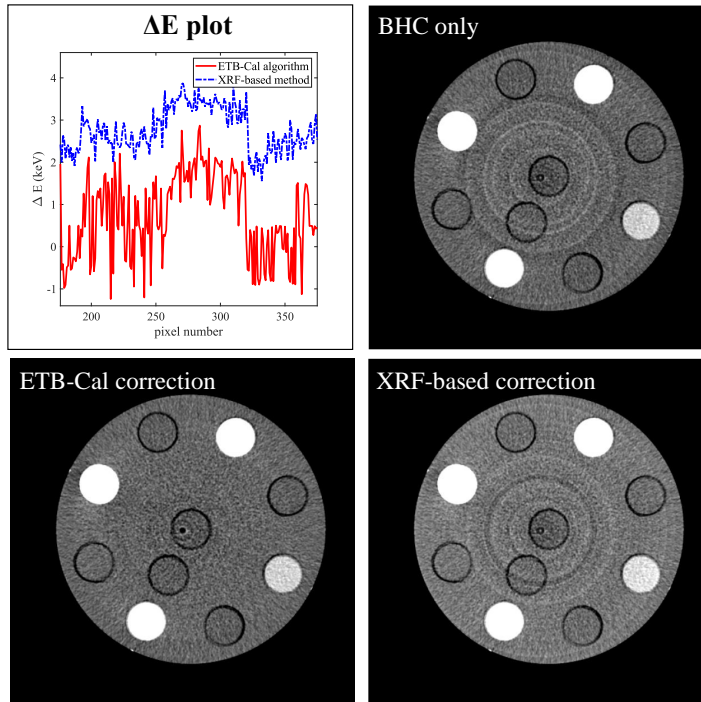


Figure 11: Result of X-ray fluorescence validation. The XRF-based correction extends the ΔE_i^k measured in the signaled area to the entire detector row and set $g_i(E)$ to 1. Display window: [920, 1080] HU.

the ring artifacts and the bony beam hardening artifacts are significantly eliminated. In the bone density image of head phantom, we selected five ROIs in the bone region for mean value statistics. The range of values relative to the smallest mean was found to be only 0.9 %, indicating that the decomposition values are both accurate and exhibit good uniformity.

4.2.4. Validation results of XRF experiment We also conducted a X-ray fluorescence experiment. The experimental setup is as shown in Fig. 4. Due to the close proximity of the metal powder placement to the detector and the relatively low production of fluorescent photons, only about 800 pixels exhibiting signals with relatively large amplitudes. We performed Gaussian peak fitting on the data from these 800 pixels, and used the peak positions obtained from the fitting as actual detector energy threshold. The difference between the fluorescence energy and the measured threshold was then calculated as the corresponding ΔE_i^k .

It can be seen in Fig. 11 that the threshold bias obtained from the fluorescence experiment shows a high degree of similarity in trend with the results obtained from our ETB-Cal algorithm. At the same time, by extending the ΔE_i^k values of the detector units at the boundary of the effective fluorescence signal region to the no effective signal region and setting the $g_i(E)$ of all detector pixels to 1, we obtain the reconstructed image with inconsistency correction based on the fluorescence experiment results. It is

evident that the ETB-Cal algorithm provides significantly better correction results than fluorescence-based one.

5. Discussion & Conclusion

In this work, we have proposed a novel approach to address spectral inconsistency in photon-counting computed tomography (PCCT) by developing a unified, two-terms factorized spectral model. Separating the spectral skew term and energy-threshold bias (ETB) analytical characterization term, this model provides an effective calculator towards ETB, which is a straightforward and computationally efficient two-step decomposition algorithm. This model as well as ETB-Cal algorithm demonstrate a capability of adaptive spectral inconsistency correction, and diminish the need for traditional, time-consuming X-ray fluorescence-based calibrations.

Our method, validated through both numerical simulations and physics experiment, performs significant improvements in PCCT image quality, with a marked reduction in inconsistency quantitative indicators (Δ_{MAX}) across a range of energy thresholds. These findings highlight the practicality and generalizability of our approach, which not only simplifies the calibration process but also ensures more reliable and accurate material decomposition in PCCT systems.

However, there are still rooms for further study to extend the spectral model established in this work to other physics effects of scattering, charge sharing, energy spreading and pulse pileup, which makes the actual spectral calibration and correction more difficult. In the follow-up work, we can try to optimize the spectral model from the underlying physics and combine with deep learning and other methods to model and correct the spectral inconsistency.

Acknowledgment

This project was supported in part by the National Key R&D Program of China (No. 2022YFE0131100), and the National Natural Science Foundation of China (No.U20A20169 and No.12075130).

Data Availability Statement

The data that support the findings of this study are available upon reasonable request from the authors.

References

- [1] T. Flohr, M. Petersilka, A. Henning, S. Ulzheimer, J. Ferda, and B. Schmidt, Photon-counting CT review, *Phys Med* **79**, 126–136 (2020).

- [2] M. Danielsson, M. Persson, and M. Sjolín, Photon-counting x-ray detectors for CT, *Phys Med Biol* **66**, 03TR01 (2021).
- [3] M. J. Willemink, M. Persson, A. Pourmorteza, N. J. Pelc, and D. Fleischmann, Photon-counting CT: Technical Principles and Clinical Prospects, *Radiology* **289**, 293–312 (2018).
- [4] Z. Yu, S. Leng, S. M. Jorgensen, Z. Li, R. Gutjahr, B. Chen, A. F. Halaweish, S. Kappler, L. Yu, E. L. Ritman, and C. H. McCollough, Evaluation of conventional imaging performance in a research whole-body CT system with a photon-counting detector array, *Phys Med Biol* **61**, 1572–95 (2016).
- [5] R. Ballabriga, J. Alozy, F. N. Bandi, M. Campbell, N. Egidos, J. M. Fernandez-Tenllado, E. H. M. Heijne, I. Kremastiotis, X. Llopart, B. J. Madsen, D. Pennicard, V. Sriskaran, and L. Tlustos, Photon Counting Detectors for X-Ray Imaging With Emphasis on CT, *IEEE Transactions on Radiation and Plasma Medical Sciences* **5**, 422–440 (2021).
- [6] P. M. Shikhaliev and S. G. Fritz, Photon counting spectral CT versus conventional CT: comparative evaluation for breast imaging application, *Phys Med Biol* **56**, 1905–30 (2011).
- [7] P. M. Shikhaliev, T. Xu, and S. Molloy, Photon counting computed tomography: concept and initial results, *Med Phys* **32**, 427–36 (2005).
- [8] S. A. Si-Mohamed, M. Sigovan, J. C. Hsu, V. Tatard-Leitman, L. Chalabreysse, P. C. Naha, T. Garrivier, R. Dessouky, M. Carnaru, L. Boussel, D. P. Cormode, and P. C. Douek, In Vivo Molecular K-Edge Imaging of Atherosclerotic Plaque Using Photon-counting CT, *Radiology* **300**, 98–107 (2021).
- [9] E. Roessl, B. Brendel, K. J. Engel, J. P. Schlomka, A. Thran, and R. Proksa, Sensitivity of photon-counting based K-edge imaging in X-ray computed tomography, *IEEE Trans Med Imaging* **30**, 1678–90 (2011).
- [10] K. Rajendran, M. Petersilka, A. Henning, E. Shanblatt, J. Marsh, J., J. Thorne, B. Schmidt, T. Flohr, J. Fletcher, C. McCollough, and S. Leng, Full field-of-view, high-resolution, photon-counting detector CT: technical assessment and initial patient experience, *Phys Med Biol* **66** (2021).
- [11] P. L. Rajbhandary, S. S. Hsieh, and N. J. Pelc, Effect of Spectral Degradation and Spatio-Energy Correlation in X-Ray PCD for Imaging, *IEEE Trans Med Imaging* **37**, 1910–1919 (2018).
- [12] E. N. Gimenez, R. Ballabriga, M. Campbell, I. Horswell, X. Llopart, J. Marchal, K. J. S. Sawhney, N. Tartoni, and D. Turecek, Study of charge-sharing in MEDIPIX3 using a micro-focused synchrotron beam, *Journal of Instrumentation* **6**, C01031–C01031 (2011).
- [13] K. Iniewski, H. Chen, G. Bindley, I. Kuvvetli, and C. Budtz-Jorgensen, Modeling charge-sharing effects in pixellated CZT detectors, 2007 Ieee Nuclear Science Symposium Conference Record, Vols 1-11 , 4608–+ (2007).

- [14] M. Kafaee and M. M. Goodarzi, Pile-Up Correction in Spectroscopic Signals Using Regularized Sparse Reconstruction, *IEEE Transactions on Nuclear Science* **67**, 858–862 (2020).
- [15] D. Leibold, S. J. van der Sar, M. C. Goorden, and D. R. Schaart, Framework for evaluating photon-counting detectors under pile-up conditions, *Journal of Medical Imaging* **11**, S12802–S12802 (2024).
- [16] T. Flohr, S. Ulzheimer, M. Petersilka, and B. Schmidt, Basic principles and clinical potential of photon-counting detector CT, *Chinese Journal of Academic Radiology* **3**, 19–34 (2020).
- [17] K. Taguchi, Energy-sensitive photon counting detector-based X-ray computed tomography, *Radiol Phys Technol* **10**, 8–22 (2017).
- [18] M.-R. Mohammadian-Behbahani and S. Saramad, A comparison study of the pile-up correction algorithms, *Nuclear Instruments and Methods in Physics Research Section A: Accelerators, Spectrometers, Detectors and Associated Equipment* **951** (2020).
- [19] R. K. Panta, M. F. Walsh, S. T. Bell, N. G. Anderson, A. P. Butler, and P. H. Butler, Energy calibration of the pixels of spectral x-ray detectors, *IEEE transactions on medical imaging* **34**, 697–706 (2014).
- [20] Y. Ge, X. Ji, R. Zhang, K. Li, and G. H. Chen, K-edge energy-based calibration method for photon counting detectors, *Phys Med Biol* **63**, 015022 (2017).
- [21] R. K. Panta, M. F. Walsh, S. T. Bell, N. G. Anderson, A. P. Butler, and P. H. Butler, Energy Calibration of the Pixels of Spectral X-ray Detectors, *IEEE Transactions on Medical Imaging* **34**, 697–706 (2015).
- [22] H. Ding, H. M. Cho, W. C. Barber, J. S. Iwanczyk, and S. Molloy, Characterization of energy response for photon-counting detectors using x-ray fluorescence, *Med Phys* **41**, 121902 (2014).
- [23] J. Cammin, J. Xu, W. C. Barber, J. S. Iwanczyk, N. E. Hartsough, and K. Taguchi, A cascaded model of spectral distortions due to spectral response effects and pulse pileup effects in a photon-counting x-ray detector for CT, *Medical Physics* **41** (2014).
- [24] J. Cammin, S. Kappler, T. Weidinger, and K. Taguchi, Evaluation of models of spectral distortions in photon-counting detectors for computed tomography, *Journal of medical imaging* **3**, 023503–023503 (2016).
- [25] P.-A. Rodesch, D. Richtsmeier, E. Guliyev, K. Iniewski, and M. Bazalova-Carter, Comparison of threshold energy calibrations of a photon-counting detector and impact on CT reconstruction, *IEEE Transactions on Radiation and Plasma Medical Sciences* **7**, 263–272 (2023).
- [26] X. Liu, H. Chen, H. Bornefalk, M. Danielsson, S. Karlsson, M. Persson, C. Xu, and B. Huber, Energy Calibration of a Silicon-Strip Detector for Photon-Counting

- Spectral CT by Direct Usage of the X-ray Tube Spectrum, *IEEE Transactions on Nuclear Science* **62**, 68–75 (2015).
- [27] W. Fang, L. Li, and Z. Chen, Removing Ring Artefacts for Photon-Counting Detectors Using Neural Networks in Different Domains, *IEEE Access* **8**, 42447–42457 (2020).
- [28] E. Y. Sidky, E. R. Paul, T. Gilat-Schmidt, and X. Pan, Spectral calibration of photon-counting detectors at high photon flux, *Med Phys* **49**, 6368–6383 (2022).
- [29] O. Lee, S. Kappler, C. Polster, and K. Taguchi, Estimation of Basis Line-Integrals in a Spectral Distortion-Modeled Photon Counting Detector Using Low-Rank Approximation-Based X-Ray Transmittance Modeling: K-Edge Imaging Application, *IEEE Trans Med Imaging* **36**, 2389–2403 (2017).
- [30] L. Okkyun, S. Kappler, C. Polster, and K. Taguchi, Estimation of Basis Line-Integrals in a Spectral Distortion-Modeled Photon Counting Detector Using Low-Order Polynomial Approximation of X-ray Transmittance, *IEEE Trans Med Imaging* **36**, 560–573 (2017).
- [31] Y. Chen, Y. Xing, and H. Gao, Physics-based modeling of energy threshold induced spectral inconsistency and its adaptive correction scheme for photon-counting CT, in *Medical Imaging 2024: Physics of Medical Imaging*, volume 12925, pages 6–10, SPIE, 2024.
- [32] R. E. Alvarez and A. Macovski, Energy-selective reconstructions in x-ray computerised tomography, *Physics in Medicine & Biology* **21**, 733 (1976).
- [33] W. Xiaoye, H. Jiang, S. Paavana, X. Dan, J. Yunnan, Y. G. Kumar, C. A. Israel, and G. Hewei, *System and method for multi-material correction of image data*, Niskayuna NY US, us9025815 edition, 2015.